CHALMERS
UNIVERSITY OF TECHNOLOGY

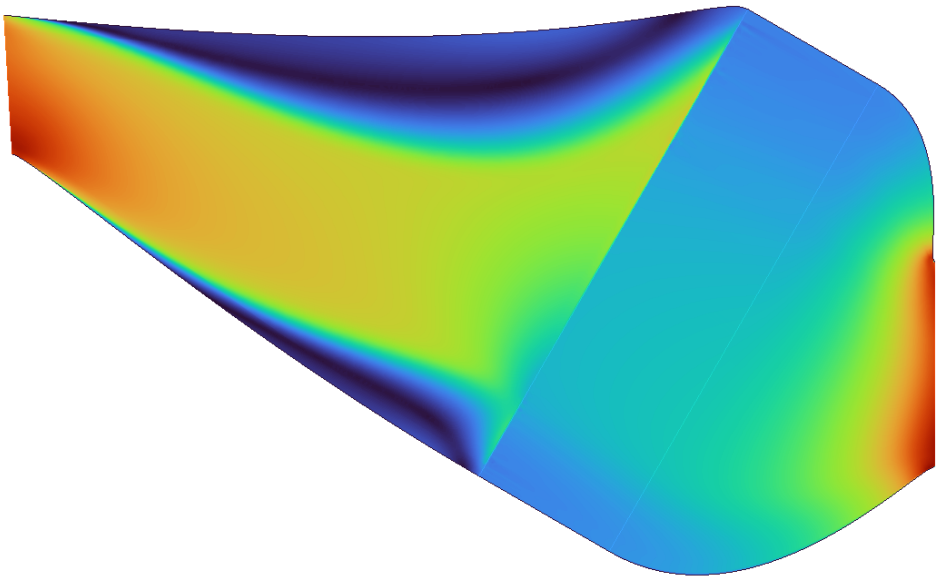

Coupled Design Optimization of Compact Heat Exchangers in Aviation

A design study using a generalized heat exchanger model, computational fluid dynamics and Bayesian optimization

Master's thesis in Applied Mechanics

ERIK HASSELWANDER

DEPARTMENT OF MECHANICS AND MARITIME SCIENCES

CHALMERS UNIVERSITY OF TECHNOLOGY
Gothenburg, Sweden 2025
www.chalmers.se

Master's Thesis in Applied Mechanics 2025

Coupled Design Optimization of Compact Heat Exchangers in Aviation

A design study using a generalized heat exchanger model, computational fluid dynamics and Bayesian optimization

ERIK HASSELWANDER

CHALMERS
UNIVERSITY OF TECHNOLOGY

Department of Mechanics and Maritime Sciences
Division of Fluid Dynamics
Chalmers University of Technology
Gothenburg, Sweden 2025

Coupled Design Optimization of Compact Heat Exchangers in Aviation
A design study using a generalized heat exchanger model, computational fluid dynamics and Bayesian optimization
ERIK HASSELWANDER

Supervisor: Petter Miltén, Department of Mechanics and Maritime Sciences, Isak Jonsson, Department of Mechanics and Maritime Sciences, and Anders Lundbladh, GKN Aerospace Sweden AB
Examiner: Carlos Xisto, Department of Mechanics and Maritime Sciences

Master's Thesis 2025
Department of Mechanics and Maritime Sciences
Division of Fluid Dynamics
Chalmers University of Technology
SE-412 96 Gothenburg
Sweden
Telephone +46 31 772 1000

Cover: Plot of velocity magnitude inside an intermediate compressor duct with an integrated heat exchanger.

Typeset in LaTeX
Gothenburg, Sweden 2025

Coupled Design Optimization of Compact Heat Exchangers in Aviation
A design study using a generalized heat exchanger model, computational fluid dynamics and Bayesian optimization
ERIK HASSELWANDER
Department of Mechanics and Maritime Sciences
Chalmers University of Technology

Abstract

The transition to hydrogen-fuelled aviation presents significant challenges in thermal management, particularly in the integration of high-performance, compact heat exchangers. As the European Union aims to achieve net-zero emissions by 2050, hydrogen-powered gas turbine engines are a promising solution. Future civil and military engines will face increased thermal loads, necessitating the integration of megawatt-class heat exchangers while maintaining aerodynamic efficiency.

This master's thesis addresses this problem through the optimization of duct geometries with integrated finned heat exchangers. The primary focus of the thesis is to investigate how performance varies with heat exchanger inlet area and total duct length. To enable an objective comparison of losses across different designs, the internal heat exchanger geometry was updated between each CFD iteration to converge the solution to a specified performance target.

The results of this study provide new insights into the underlying trade-offs. Heat exchangers with a larger area result in lower losses over the heat exchanger matrix but incur increased losses in the ducts. Additionally, shorter ducts lead to higher losses over the heat exchanger due to the reduced diffusive capacity, while duct losses remain largely unchanged. Another notable trend in the optimized designs is the presence of significant recirculation regions in all duct geometries, highlighting the strong diffusive capacity of the heat exchanger.

The study also includes a limited investigation into the effects of the transversal fins of the heat exchanger by selecting a fixed geometry from the previous optimization trials and removing the sink term associated with the fins. This modification increases the normalized losses from 1.35 to 1.37, indicating that the pressure drop across the heat exchanger matrix is the primary driver of diffusion, rather than the finned structure itself.

Keywords: hydrogen aviation, heat exchanger integration, thermal management, CFD simulation, aerothermal integration.

Acknowledgements

I would like to thank my examiner, Carlos Xisto, and my supervisors, Isak Jonsson, Petter Miltén, and Anders Lundbladh, for their invaluable help and support throughout this work. All of you have gone above and beyond what is expected in your roles to ensure that I had the best possible conditions for success and I am extremely thankful for this.

Furthermore, I would like to thank my friends and family who have supported me throughout this work. I would not have been able to finish this work without your continuous support.

Erik Hasselwander, Gothenburg, June 2025

List of Acronyms

Below is the list of acronyms that have been used throughout this thesis listed in alphabetical order:

AR	Area Ratio
GGP	Generalized Geometry Parameter
HEX	Heat EXchanger
ICD	Intermediate Compressor Duct
RANS	Reynolds-averaged Navier-Stokes

Nomenclature

Below is the nomenclature of indices, sets, parameters, and variables that have been used throughout this thesis.

Indices

i,j	Indices for spatial dimensions
c	Index for the cold side of the HEX
h	Index for the hot side of the HEX
r	Index for the ratio between the hot and cold side of the HEX
0	Index for total flow quantity
f	Index for fin properties of the heat exchanger

Parameters

A	Area
U	Heat transfer coefficient
L	Length
χ	Solid volume fraction
σ	Void fraction
α	Surface area density
V	Volume
k	Thermal conductivity
η_0	Surface efficiency
η_f	Fin efficiency
ℓ	Undisturbed flow length
D_h	Hydraulic diameter
f	Friction factor

j	Colburn factor
ΔR	Change in mean radius
λ	Geometry control parameter
κ	Heat exchanger tilt angle
ψ	Under relaxation factor

Variables

u	Velocity
T	Temperature
q	Heat transfer rate
t	Thickness
μ	Dynamic viscosity
ρ	Density
p	Pressure
x, r, y	Spatial coordinates
φ	Velocity non-uniformity

Contents

List of Figures

List of Tables

1
Introduction

1.1 Background

Aviation accounted for 3.8 % to 4 % of the greenhouse gas emissions in 2022. As part of the European Union's goal to reach net-zero emissions in the union by 2050 [1], the transport sector emissions have to be reduced by 90 % [2]. The aviation sector is currently the second largest contributor to emissions in the transport sector, and to be able to achieve this goal drastic and innovative changes are required in the aviation sector. One proposed solution to this problem is the use of hydrogen fuel, as it is renewable and can be sustainably produced while having CO_2-free combustion.

The use of cryogenic hydrogen as a fuel source presents numerous opportunities for innovative propulsion system designs. One such opportunity lies in utilizing the cryogenic properties of liquid hydrogen for thermal management within the engine itself. Recent studies have explored various methods for integrating cryogenic hydrogen into engine cooling strategies, including the use of cooled compressor vanes [3], intercooling systems [4, 5, 6], and recuperators [4]. These approaches aim to improve thermal efficiency and overall engine performance by leveraging the large cooling capacity of liquid hydrogen.

Previous research has demonstrated that the incorporation of intercooling alone can lead to a reduction in specific fuel consumption (SFC) of approximately 3%, while combining intercooling with a recuperator can yield reductions of up to 6% [4]. These findings highlight the potential benefits of integrating cryogenic cooling technologies into advanced propulsion systems.

1.2 Purpose

The primary purpose for this thesis is to investigate a potential design for an intermediate compressor duct (ICD) with an integrated heat exchanger (HEX), intended for implementation in the Chalmers 2.5 stage experimental low pressure compressor facility. In addition to the physical design, this work aims to further develop and refine the computational tools and methodologies used in the design process. The proposed configuration is specifically developed to facilitate experimental validation of the numerical models employed, thereby supporting the accuracy and reliability of the simulation-based design approach.

1.3 Goals

The main objective of this thesis is to advance the development of a computational design tool for the design generation of ICDs with embedded heat exchangers. A key aspect of this development is the incorporation of a generalized heat exchanger model capable of accurately representing aerothermal performance within a continuum-based modeling framework. In addition, the thesis seeks to present a conceptual design suitable for implementation and validation within the Chalmers test facility, thereby contributing to the verification of the proposed modeling approach.

1.4 Limitations

Several assumptions and simplifications are adopted throughout this work. The duct and heat exchanger are modeled using a two-dimensional, axisymmetric, steady-state approach, primarily due to the high computational cost associated with the optimization process. Moreover, the study is confined to a single integration case, defined by specific boundary conditions and geometric constraints posed by the experimental setup, to limit the parameter space and facilitate a more in-depth analysis of the proposed methodology.

2
Theory

This chapter briefly presents the theory used in this work. This consists of three main ideas: The Navier-Stokes equations used to solve the fluid flows, the GenHEX method to calculate aerothermal performance for heat exchangers and Bayesian optimization.

2.1 Navier-Stokes

The Navier-Stokes equations are a set of equations that govern the motion of fluids. The equations can be written on index notation as

$$\frac{\mathrm{d}\rho}{\mathrm{d}t} + \rho\frac{\partial u_i}{\partial x_i} = 0 \tag{2.1}$$

$$\rho\frac{\mathrm{d}u_i}{\mathrm{d}t} = -\frac{\partial p}{\partial x_i} + \frac{\partial}{\partial x_j}\left(\mu\left[\frac{\partial \bar{u}_i}{\partial x_j} + \mu\frac{\partial \bar{u}_j}{\partial x_i}\right] - \frac{2}{3}\frac{\partial u_k}{\partial x_k}\delta_{ij}\right) + \rho f_i \tag{2.2}$$

where ρ is the fluid density, u_i is the fluid velocity, μ is the dynamic viscosity, p is the pressure and f_i are body forces.

Solving these equations directly is referred to as direct numerical simulations. To get accurate results while directly from these equations requires a large computational mesh, especially for high-speed applications, which require large computational resources even for simple cases.

2.1.1 Reynolds averaged Navier-stokes

The Reynolds-averaged Navier-Stokes (RANS) equations are commonly used to reduce the computational power required to solve the incompressible Navier-stokes equations by time-averaging. The equations are derived by decomposing the velocity into two terms as

$$u_i = \bar{u}_i + u_i' \tag{2.3}$$

where the first term is the time-averaged component and the second term is a fluctuating component. By inserting this into the Navier-Stokes equations and time-averaging the RANS equations are obtained as

$$\frac{\partial \bar{u}_i}{\partial x_i} = 0 \tag{2.4}$$

$$\rho\bar{u}_j\frac{\partial \bar{u}_i}{\partial x_j} = \frac{\partial}{\partial x_j}\left[-\bar{p}\delta_{ij} + \mu\left(\frac{\partial \bar{u}_i}{\partial x_j} + \frac{\partial \bar{u}_j}{\partial x_i}\right) - \rho\bar{u_i'u_j'}\right], \tag{2.5}$$

where the time-averaged velocity field, u_i, is solved for.

The RANS equation are however not closed due to the Reynolds stress term $-\rho\bar{u_i'u_j'}$. To close the equations and solve the RANS equations a model is needed for this non-linear term, as the fluctuations are not solved for directly in RANS. A common approach to this closure problem is the Shear Stress Transport (SST) $k-\omega$ turbulence model which is the model used in the present work.

2.2 Generalized heat exchanger method

The equation governing heat transfer from the hot fluid to the cold fluid in a heat exchanger is

$$\frac{dq}{dA} = U(T_h - T_c) \tag{2.6}$$

where q is the heat transfer rate, T_h and T_c are the hot and cold fluid temperatures respectively and U is the heat transfer coefficient. For a given problem where the temperatures and geometry is known, as is the case for CFD applications, the only unknown in the equation above is the conductance.

Correlations for the heat transfer coefficient for a vast number of heat exchangers exists. As this study aims to keep the thermal load constant by changing the geometrical properties of a heat exchanger there is a need for a generalized model. One such model is the generalized heat exchanger, *GenHEX*, method[6]. The method consists of two main ideas: a framework to generalize heat exchanger geometries and a general correlation to estimate the performance based on those geometries.

The convention in this thesis is to denote the hot and cold fluids with sub-indices h and c respectively.

2.2.1 Generalized geometry

This section contains a compact overview of the relevant details of the generalized geometry as proposed in [6]. For the complete geometrical formulation the reader is referred to the original source.

The generalized geometry consists of eight parameters: three to define the outer dimensions of the heat exchanger, L_x, L_y and L_z, two structural parameters, t_W and t_f, and three geometrical generalization parameters (GGPs), σ_r, α_r and χ.

The parameters of interest in this thesis are the GGPs. χ is the solid volume fraction, V_s/V_t, which controls the amount of solid volume, for instance finned structures, in the geometry. σ is the void fraction, A_{ff}/A_{fr} which controls the amount of fluid flow available. Lastly α is the surface area density, A_w/V_t which controls the amount of surface area in each fluid. Figure 2.1 shows how the heat exchanger geometry changes with the GGPs.

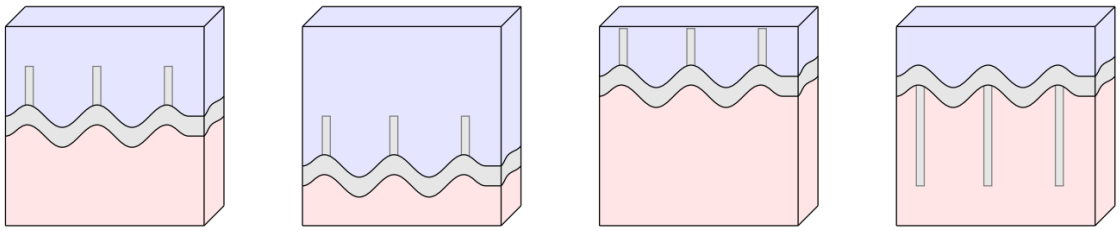

(a) $\sigma_r \approx 1$, $\alpha_r < 1$ (b) $\sigma_r < 1$, $\alpha_r < 1$ (c) $\sigma_r > 1$, $\alpha_r < 1$ (d) $\sigma_r > 1$, $\alpha_r > 1$, χ increased

Figure 2.1: General representation of a heat exchanger geometry for some combinations of the geometrical generalization parameters. Figure from [6].

The ratios $\sigma_r = \sigma_c/\sigma_h$ and $\alpha_r = \alpha_c/\alpha_h$ can also be formed. It can be shown that σ_h and α_h can be expressed as functions of χ, σ_r, α_r and the average structural thickness t as

$$\sigma_h = \frac{1-\chi}{\sigma_r + 1} \tag{2.7}$$

and

$$\alpha_h = \frac{2\chi}{t\,(\alpha_r + 1)}. \tag{2.8}$$

2.2.2 Estimated performance

The heat transfer coefficient U for the hot fluid side can be rewritten using the generalized geometric parameters above as

$$\frac{1}{U_h} = \frac{1}{\eta_{o,h} h_h} + \frac{\alpha_r}{\eta_{o,c} h_c} + \frac{2t}{\left(1 + \frac{1}{\alpha_r}\right) k} \tag{2.9}$$

where k is the thermal conductivity of the heat exchanger material, η_o is the overall surface efficiency and h is the heat transfer coefficient for convection for the respective fluids as indicated by the indices[6].

The overall surface efficiency is 100% for the heat exchanger side without fins. For fluids interacting with fins the overall surface efficiency will be lower as there will be a temperature gradient along the fins which reduces the temperature effectiveness[7]. This reduction can be calculated, assuming the hot side is finned, as

$$\eta_{o,h} = 1 - \frac{A_h}{A}(1 - \eta_f) = 1 - \sigma_{ftt,h}\eta_{f,h} \tag{2.10}$$

where η_f can be determined from relations depending on the fin geometry. For straight fins with constant cross section the fin efficiency can be calculated as

$$\eta_{f,h} = \frac{\tanh\left(ml_h\right)}{ml_h} \tag{2.11}$$

where

$$ml_h = \frac{l_f}{\sqrt{t_f}}\sqrt{\frac{2h_h}{k}}. \tag{2.12}$$

To be able to calculate U for a given geometry the heat transfer coefficient for convection h has to be obtained. This is obtained through the Nusselt number which is defined as

$$\mathrm{Nu} = \frac{4h\sigma}{\alpha k} = j\mathrm{RePr}^{1/3} \tag{2.13}$$

where the first equality is the common definition of the Nusselt number and the second equality is the Chilton-Colburn analogy and the Reynolds number Re is defined, through a heat exchanger length scale equal to the hydraulic diameter $D_h = 4\frac{\sigma}{\alpha}$, as

$$\mathrm{Re} = \frac{4\rho u\sigma}{\alpha\mu} \tag{2.14}$$

and the Prandtl number Pr is defined as

$$\mathrm{Pr} = \frac{c_p\mu}{k}. \tag{2.15}$$

Reordering equation 2.13 gives an expression for h, for the hot side, as

$$h = \frac{k\alpha_h\mathrm{Nu}}{4\sigma_h} = \frac{k\alpha_h j\mathrm{RePr}^{1/3}}{4\sigma_h} \tag{2.16}$$

where the only unknown is the Colburn factor j, and thus the only unknown to calculate the heat transfer coefficient U is also the Colburn factor.

The pressure losses are calculated as

$$\Delta p_0 = \frac{\dot{m}^2}{2\rho_{in}A_{fr}^2}\left(\left(\frac{1}{\sigma^2}+1\right)\left(\frac{\rho_{in}}{\rho_{out}}-1\right)+2fL\frac{\alpha}{\sigma^3}\frac{\rho_{in}}{\rho_m}\right) \tag{2.17}$$

where L is the length of the heat exchanger in the flow direction and f is the Fanning friction factor[8]. The only unknown variable in equation 2.17, for a given flow and geometry, is the friction factor f.

To be able to calculate the heat transfer coefficient and pressure losses the Colburn factor j and friction factor f need to be obtained. The following correlations for a general heat exchanger are presented in [6]:

$$j = 0.360\left(\frac{\ell}{D_h}\right)^{-0.401}\mathrm{Re}^{-0.413} + 2.13\times10^{-5}\left(\frac{\ell}{D_h}\right) \tag{2.18}$$

and

$$f = 0.492\left(\frac{\ell}{D_h}\right)^{-0.501}\mathrm{Re}^{-0.232} \tag{2.19}$$

where ℓ is the undisturbed flow length. The undisturbed flow length for straight continuous fins is equal to the length of the fins.

2.3 Bayesian optimization

The content of this section draws significantly from the work by Morita *et al.* [9]. While the presentation has been adapted to fit the context of this thesis, the core

concepts and explanations closely follow the original publication. Therefore, individual citations within this section are omitted unless otherwise specified.

Bayesian optimization (BO) is a gradient-free optimization method particularly suited for problems where evaluations of the objective function are expensive, noisy, or lack an analytical form. The Bayesian aspect of the method arises from the use of a probabilistic surrogate model, which is sequentially updated as new evaluations are obtained. This surrogate model enables informed decisions about where to sample next by balancing exploitation, which involves sampling where the model predicts high performance, and exploration, which involves sampling in regions of high uncertainty.

Let the design parameters be defined as a vector $\mathbf{q} = \{q_1, q_2, \ldots, q_n\} \in \mathbb{R}^n$, which are subject to variation. The objective is to find the set of parameters that minimizes a target function $r(\mathbf{q})$, which may be noisy or computationally expensive to evaluate. This problem can be stated as:

$$\mathbf{q}_{\text{opt}} = \arg\min_{\mathbf{q}} r(\mathbf{q}). \tag{2.20}$$

In many practical applications—such as those involving computational fluid dynamics (CFD)—the objective function is treated as a black box and may exhibit noise. In such cases, a surrogate model $\tilde{f}(\mathbf{q})$ is constructed to approximate the behavior of $r(\mathbf{q})$ while quantifying uncertainty.

Bayesian optimization relies on two key components: the surrogate model and the acquisition function. The surrogate model approximates the true objective function; in this work, Gaussian process regression is used for this purpose, as it provides both a mean prediction and a quantification of uncertainty. The acquisition function determines the next point in the design space to evaluate by balancing exploitation and exploration. In this thesis, the Expected Improvement criterion is used as the acquisition strategy. Together, these components enable efficient optimization of expensive and noisy functions, making Bayesian optimization well suited to the problems addressed in this work.

2.3.1 Gaussian Process Regression

Gaussian Process Regression is a non-parametric, Bayesian approach to regression that models the distribution over possible functions that fit the observed data. A Gaussian process is fully specified by a mean function $m(\mathbf{q})$ and a covariance function $c(\mathbf{q}, \mathbf{q}'; \Theta_\varepsilon, \beta)$, and is written as

$$f(\mathbf{q}) \sim \mathcal{GP}(m(\mathbf{q}), c(\mathbf{q}, \mathbf{q}'; \Theta_\varepsilon, \beta)). \tag{2.21}$$

The mean and covariance functions are defined as

$$m(\mathbf{q}) = \mathbb{E}[\tilde{f}(\mathbf{q})], \tag{2.22}$$

$$c(\mathbf{q}, \mathbf{q}'; \Theta_\varepsilon, \beta) = \mathbb{E}[(\tilde{f}(\mathbf{q}) - m(\mathbf{q}))(\tilde{f}(\mathbf{q}') - m(\mathbf{q}'))]. \tag{2.23}$$

In these definitions, Θ_ε denotes the parameters defining the noise structure, and β represents the hyperparameters of the model.

Given a set of observations $\mathcal{D} = \{\mathbf{Q}, \mathbf{y}\}$, where $\mathbf{Q}$ are input samples and $\mathbf{y}$ the corresponding outputs, the Gaussian process defines a predictive distribution at a new point $\mathbf{q}_*$ in terms of a mean $\mu(\mathbf{q}_*)$ and variance $\sigma^2(\mathbf{q}_*)$. These quantities are computed using the covariance function and reflect both the expected value of the function and the model's uncertainty at that location.

2.3.2 Expected Improvement

To select the next sampling point $\mathbf{q}^{k+1}$, the acquisition function *Expected Improvement* (EI) is employed. For a minimization problem, the expected improvement at a candidate point $\mathbf{q}$ is defined as

$$\mathrm{EI}(\mathbf{q}) = \mathbb{E}\left[\max\Big(0, r_{\mathrm{best}} - \tilde{f}(\mathbf{q})\Big)\right], \tag{2.24}$$

where r_{best} denotes the best (lowest) observed value of the objective function after k iterations.

When the surrogate model $\tilde{f}(\mathbf{q})$ is a Gaussian process with predictive mean $\mu(\mathbf{q})$ and standard deviation $s(\mathbf{q})$, the expected improvement can be expressed in closed form as

$$\mathrm{EI}(\mathbf{q}) = \left(r(\mathbf{q}_{\mathrm{best}}) - m(\mathbf{q})\right)\Phi(\zeta) + s(\mathbf{q})\,\phi(\zeta), \tag{2.25}$$

where

$$\zeta = \frac{r(\mathbf{q}_{\mathrm{best}}) - m(\mathbf{q})}{s(\mathbf{q})}, \tag{2.26}$$

and $\Phi(\zeta)$ and $\phi(\zeta)$ denote the cumulative distribution function and probability density function of the standard normal distribution, respectively.

In Equation 2.25, the first term represents exploitation, favoring points with predicted values better than the current best, while the second term encourages exploration by prioritizing points with high uncertainty. This balance enables efficient search for the global minimum by guiding sampling towards regions most likely to improve the objective.

3
Methods

This chapter describes the methodology used to design intermediate compressor ducts with integrated heat exchangers. The duct was designed for use in the Chalmers 2.5 stage low pressure compressor test rig which put forth several design constraints. This is expressed through geometric and flow boundary conditions as well as the use of water as the cooling agent.

Section 3.1 first introduces the geometry of the duct and heat exchanger, followed by the CFD modeling used in Section 3.2. Thereafter the optimization setup is explained. Lastly the validation cases used to validate the model against experimental diffusing ducts are presented.

3.1 Geometry

The overall geometry considered in this study comprises a diffusing duct, a contracting duct, and the respective hot (air) and cold (water) sides of the heat exchanger. Representative geometries for the hot and cold side ducts are shown in Figures 3.1a and 3.1b, respectively. These figures illustrate the meridional plane of the system, as the duct geometries are fully axisymmetric. The geometries are revolved around the dashed line.

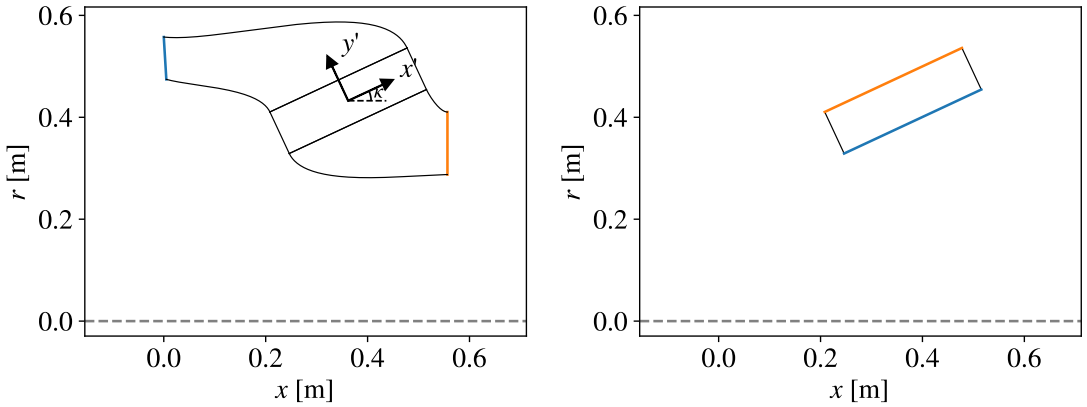

(a) Air side (hot) **(b)** Water side (cold)

Figure 3.1: Meridional view of an intermediate compressor duct with an integrated heat exchanger. The blue lines represents the respective domain inlets and the orange lines represent the outlets.

Each duct comprises two splines that connect the inlet and outlet to the heat

exchanger, one spline at the shroud and one at the hub. The air and water sides of the heat exchanger share the same bounding geometry which allows for the direct calculation of the temperature difference between the two sides of the heat exchanger.

The inlet corner points were constrained by the outlet duct geometry of the Chalmers 2.5-stage compressor test rig. As the test rig consists of only a single compressor, and thus has nothing downstream of the duct, there were no fixed outlet corner points or duct length constraints imposed by the existing setup.

The outlet corner points were chosen to maintain the same cross-sectional area as the inlet, while reducing the mean radius. The mean radius was reduced as $R_{inlet} - R_{outlet} = \Delta R = 0.2\,\mathrm{m}$, which is a typical value for engines of this size. The heat exchanger length was set to $L_x = 0.09\,\mathrm{m}$, consistent with the configuration used in [4, 5].

The overall duct length was determined using the engine duct parameter $\Delta R/L$, defined as the ratio between the change in mean radius from inlet to outlet and the total length of the duct. Aggressive designs typically exhibit values above 0.6, while more conventional designs fall around 0.5 or below. In this study, a baseline value of $\Delta R/L = 0.3$ was selected to achieve a conservative duct design capable of accommodating the heat exchanger within the duct.

3.1.1 Geometry parameterization

The geometry is parameterized through 11 variables that relate to the heat exchanger and duct geometries. The parameters are illustrated in the geometry in Figure 3.2. Three parameters, x_{hex}, y_{hex} and κ, control the location and angle of the heat exchanger. The remaining eight parameters, λ_1 through λ_8, control the position of the control points for the splines that define the duct walls.

Figure 3.2 shows the bounds of the control points as the dashed lines, the dots are the position of the control points for $\lambda_n = 0.25$ and the dashed square in the center is the bounding box for the midpoint of the heat exchanger.

The black points associated with each curve, as well as the start and end points of the curve are used to generate the curves as Bézier curves. The length of the dashed lines are a fraction of the length between the corner points of the curves, determined by λ. The angle of the dashed lines are tangential to the connecting curves as this ensures a smooth transition between the curves.

In order to account for the orientation of the heat exchanger within the system, a rotated coordinate system, denoted as the x'–y' coordinate system, is introduced. This coordinate system is shown in Figure 3.1a. This local coordinate system aligns with the geometric orientation of the heat exchanger and is defined by a rotation of an angle κ relative to the global x–r coordinate system. The transformation between the global and rotated coordinate systems is expressed as

$$\begin{bmatrix} x' \\ y' \end{bmatrix} = \begin{bmatrix} \cos\kappa & \sin\kappa \\ -\sin\kappa & \cos\kappa \end{bmatrix} \begin{bmatrix} x \\ r \end{bmatrix}. \tag{3.1}$$

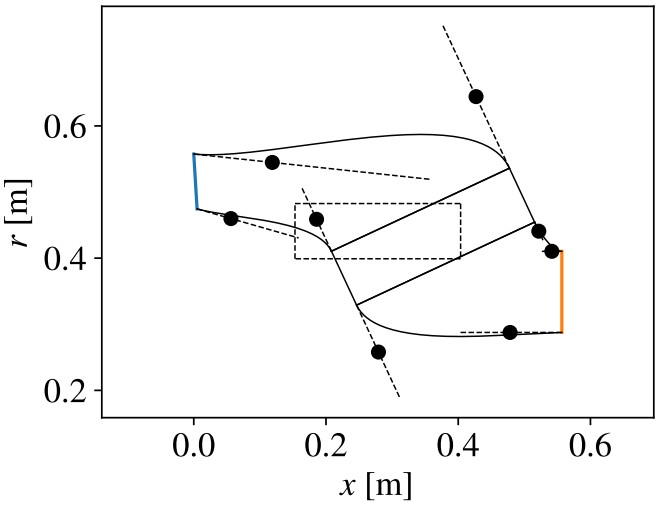

Figure 3.2: The parametrized geometry.

3.1.2 Post processing definitions

To be able to distinguish between different types of losses the duct and heat exchanger is split into four zones: diffusing duct, HEX entry, HEX core and contracting duct. The zone boundaries are defined as in Figure 3.3. The diffusing duct losses are calculated between line 1 and 2, HEX entry losses are calculated between line 2 and 3, HEX core losses are calculated between line 3 and 4, and the contracting duct losses between line 4 and 5. Line 2 is located 4.5 mm upstream of the ICD-HEX interface and line 3 is located 4.5 mm downstream of the ICD-HEX interface, or 5 % of the HEX total length in either direction of the interface.

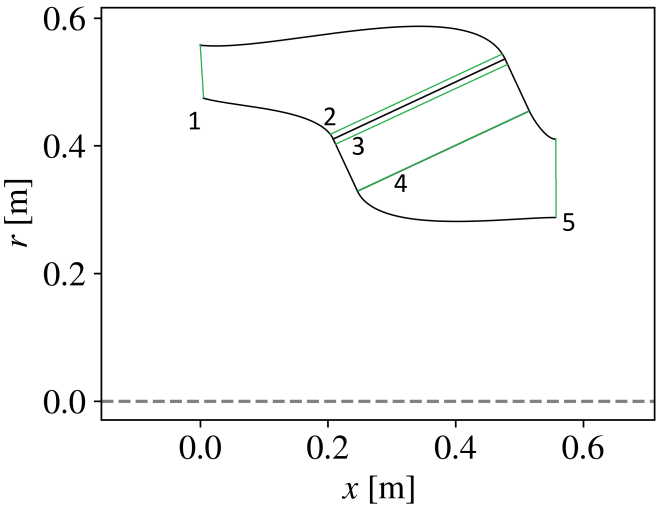

Figure 3.3: The boundaries, in green, used to distinguish between different sources of losses.

The non-uniformity of the velocity normal to the heat exchanger inlet (the y'-

direction), denoted φ, is calculated as

$$\varphi = \frac{\sum_f |u_{y',f} - \bar{u}_{y'}| A_f}{2|\bar{u}_{y'}| \sum_f A_f} \tag{3.2}$$

where $\sum_f$ represents the sum over all face, $\bar{u}_{y'}$ is the surface average of $u_{y'}$, $u_{y',f}$ denotes the velocity at the face and A_f is the area of a face. The non-uniformity is a measure used to estimate the degree of diffusion that is achieved at the heat exchanger inlet. For a uniform distribution of velocities the non-uniformity has a value of 0, which increases as the distribution becomes less uniform.

3.1.3 Heat exchanger

A reference heat exchanger is used to obtain the geometrical parameters needed to calculate the aerothermal performance (detailed in Section 3.2.3. The geometrical parameters of the cold side of the reference heat exchanger is kept constant, while the hot side is allowed to vary in order to match a target temperature drop (detailed in Section 3.2.4).

The reference heat exchanger used in this thesis is the 9.1-0.737-S finned flat-tube type, illustrated in Figure 3.4. The cold side of the heat exchanger consists of the flat tubes while the hot side consists of the fins. When matching a target temperature drop the spacing of the fins is varied by changing χ.

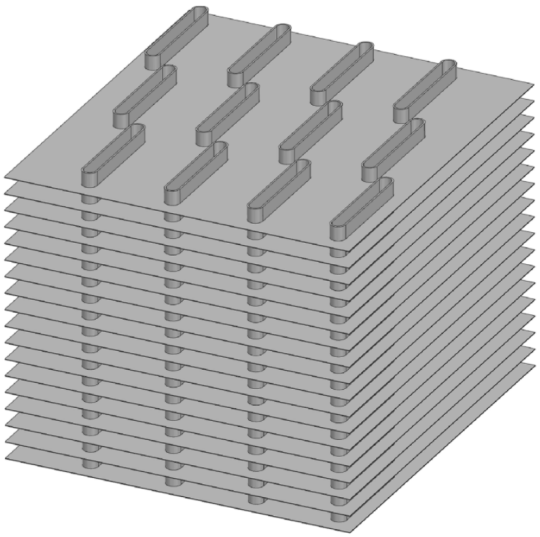

Figure 3.4: 3D-view of the 9.1-0.737-S heat exchanger geometry. Figure from [4].

Due to the unavailability of hydrogen in the experimental setup, water is employed as the working fluid on the cold side of the heat exchanger. While cryogenic hydrogen is the intended coolant for hydrogen aircraft water serves as a practical and accessible substitute for experimental validation. Its use enables assessment of both the thermal and aerodynamic performance of the heat exchanger under controlled laboratory conditions, providing a basis for extrapolation to hydrogen-based systems.

The heat exchanger is oriented such that the normal vector of the fins aligns with the x'-axis, while the flat tubes are aligned along the y'-axis. This coordinate system, denoted as x'-y', is defined in Section 3.1.1.

The heat exchanger parameters were obtained from [7]. They were then translated into GGPs to enable estimation of the aerothermal performance. The GGPs are detailed in Table 3.1. The cold side GGPs σ_c and α_c are constant, while the hot side GGPs σ_h and α_h are calculated using Equations 2.7 and 2.8.

Table 3.1: GGP Parameters for the 9.1-0.737-S heat exchanger.

Symbol	Value
Constant	
σ_c	0.01
α_c	$160\,\mathrm{m}^{-1}$
Initial values	
χ	0.231
α_h	$2151\,\mathrm{m}^{-1}$
α_r	13.45
σ_h	0.7589
σ_r	75.89

3.2 CFD modeling

The simulations are carried out using the commercial finite volume code `STAR-CCM+ 2410` using a two dimensional, axisymmetric and steady state framework. Two flow fields are solved simultaneously: the air side of the duct, which include the ducts and heat exchanger, and the water side, which includes only the heat exchanger portion of the geometry.

3.2.1 Numerics - air region

The air side is modeled as a dry compressible ideal gas. The governing equations are the compressible RANS coupled with the $k-\omega$ SST turbulence model and the energy equation. These equations are solved using a coupled solver with second-order numerical schemes. The temperature dependency of the viscosity is modeled using Sutherland's law. A compressible model was chosen even though the Mach number in this study is below 0.3 as the purpose of this work is to validate the model for use in engine conditions where the Mach number is typically in the range of $0.4-0.6$.

The inlet boundary conditions are specified using a total pressure profile, a total temperature profile, and a velocity direction specification. A previous three-dimensional RANS study has been conducted for a different ICD [10], which is used to obtain the inlet boundary conditions for the present study. The outlet boundary condition is specified as a constant pressure outlet which is updated every iteration to match the target mass flow.

These quantities were obtained by circumferentially averaging the quantities at the interface where the outlet duct meets the ICD, the dashed line in Figure **??**. The profiles used are shown in Figure 3.5 and related averaged flow properties and relevant physical quantities are shown in Table 3.2.

Table 3.2: Summary of inlet boundary conditions.

Parameter	**Value**
Total temperature, T_0	291.73 K
Total pressure, p_0	98.9 kPa
Reynolds number, Re	366 262
Mach number, Ma	0.129
Velocity, v	44.13 m s^{-1}
Blockage ratio, B_T	24 %

3.2.2 Numerics - water region

The water side of the heat exchanger is modeled as a laminar counterflow configuration with slip wall boundary conditions. In this configuration, the coolant flows in the direction opposite to that of the fluid being cooled, as indicated by the reversed inlet and outlet positions in Figures 3.1a and 3.1b. This approach is justified by the fact that multiple passes of cross flow through tubes can be reasonably approximated as a counterflow. Furthermore, this modeling strategy reduces the computational cost associated with resolving individual flow paths, while still conserving the total mass flow rate and temperature of the water.

This approach enables the determination of the temperature and velocity required to calculate the heat transfer coefficient for convection on the water side of the heat exchanger. It also allows the calculation of the temperature difference between the two fluids.

The inlet is specified as a uniform mass flow inlet with a mass flow rate of 3 kg s^{-1} and a temperature of 278.15 K (5 °C), while the outlet is a simple outflow outlet. Heat transfer is modeled as an energy sink term, equal in magnitude and opposite in sign to the energy source term applied on the air side.

3.2.3 Discretized heat exchanger model

The discretized heat exchanger model is based on the GenHEX method as desribed in Section 2.2. The method is discretized by treating each individual cell as a tiny heat exchanger with local values of U, ΔT and Δp_0. In each cell the heat transfer coefficient and pressure drop terms are calculated according to Equations 2.9 and 2.17 respectively.

The heat transfer rate, Equation 2.6, is integrated and divided by the cell volume to obtain the volumetric heat transfer rate q_h/V,

$$\frac{q_h}{V} = U\alpha_h \left(T_c - T_h\right), \tag{3.3}$$

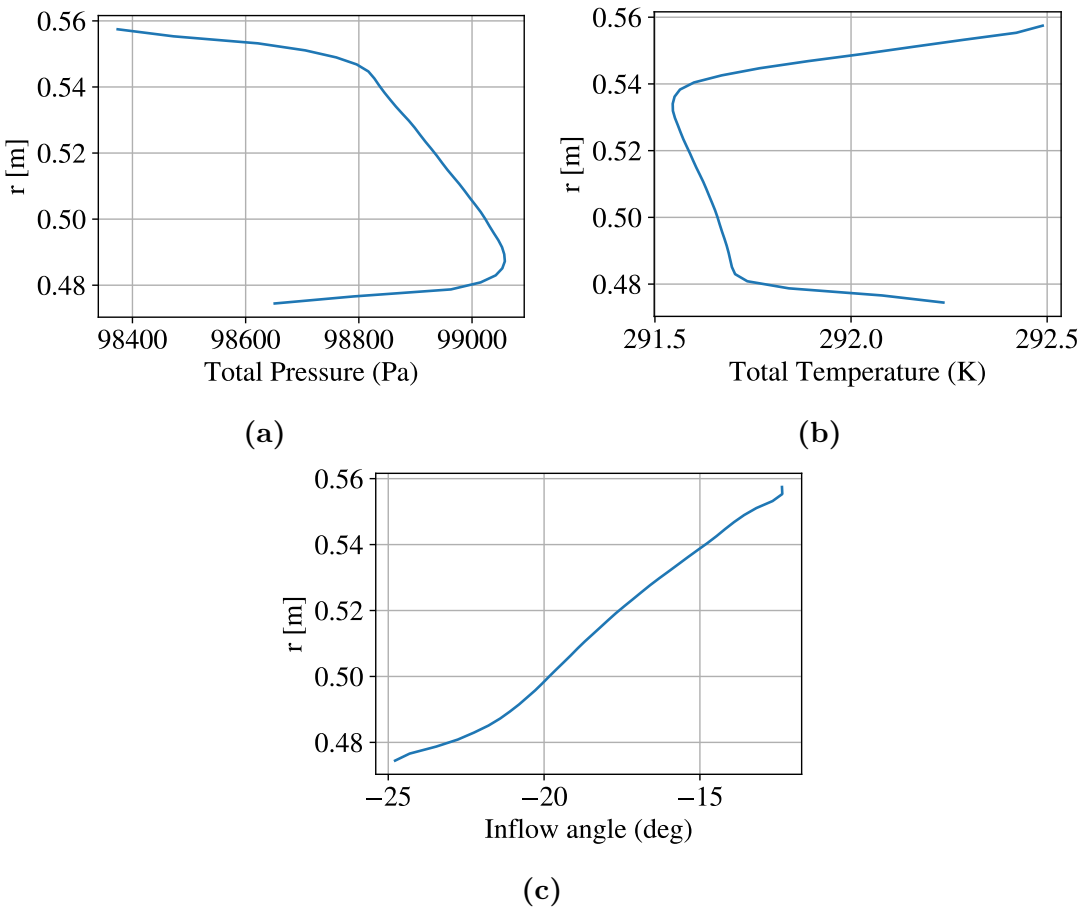

Figure 3.5: Inlet profiles to the ICD. The figure shows total pressure (a), total temperature (b) and inflow angle (c). The inflow angle is measured against the axial axis.

where the temperatures and U are calculated using Equation 2.9, based on the local flow properties in each cell. Since the CFD-computed velocity u^* does not account for the reduced flow area caused by the heat exchanger structure, it is corrected to obtain the actual velocity in the heat exchanger as

$$u = \frac{u^*}{\sigma}. \tag{3.4}$$

The calculated volumetric heat transfer rate is then applied as a source term in the energy equation for the air region and as a sink term of equal magnitude in the water region.

By assuming that the local variations of density is small, which is valid for a sufficiently fine mesh, we obtain that $\rho_{in} = \rho_{out} = \rho_m$ which allows us to rewrite Equation 2.17 as

$$\frac{\Delta p_0}{L} = \frac{u^2 \alpha \rho f}{2\sigma^3} \tag{3.5}$$

as $\dot{m} = \rho u A_{fr}$. The pressure loss term is normalized by L, to be applied as a pressure loss term in the x' and y' directions through `STAR-CCM+`'s porous region inertial resistance. The fins in the heat exchanger does not allow flow in the x' direction.

This is captured by increasing the pressure drop in the fin-normal direction, x', by a factor 1000 [4]. For the case study of an isotropic heat exchanger the pressure loss term is set according to Equation 3.5 in both directions.

3.2.4 Matching a target temperature drop

To be able to compare the designs in the optimization loop the thermal load of the heat exchanger is kept constant. This was achieved by numerically changing the spacing of the fins in the heat exchanger until a target temperature drop between the inlet and outlet is reached. To numerically change the spacing the value of χ is updated every iteration. Increasing or decreasing χ changes σ_h and α_h according to Equations 2.7 and 2.8 which in turn causes the heat transfer and pressure drops to change.

After each iteration of the flow solver a new value of χ is calculated as

$$\chi = \chi_{\text{old}} \left(1 - \psi \frac{\Delta T_{\text{current}} - \Delta T_{\text{target}}}{\Delta T_{\text{target}}} \right) \tag{3.6}$$

where $\Delta T_{current}$ is the current temperature drop, ΔT_{target} is the target temperature drop, ψ is an under relaxation factor which is used to tune the convergence. It can be seen that χ becomes constant as $\Delta T_{\text{current}} \rightarrow \Delta T_{\text{target}}$.

3.2.5 Numerical Mesh

The mesh is a polyhedral mesh with prism layers close to the wall. To ensure that the mesh is sufficiently fine close to the wall for a multitude of different designs the first layer height was chosen to be 1×10^{-6} m. The bulk of the mesh was generated using a polygonal mesher. The base size of the mesh was determined from a mesh convergence study, shown in Section 4.2.1, which resulted in meshes with approximately 60000 cells.

3.2.6 Solution convergence

The simulations were converged in two steps. 400 iterations without updating χ is first run to allow the flow field to stabilize. Thereafter the updating of χ is turned on as detailed above. The simulation is terminated when all the residuals have reduced by a factor of 1×10^6. If the simulation has not converged after a total of 1500 iterations the simulation is stopped as the residuals were observed to have stabilized after this. The simulations were discarded if the residuals are reduced by less than a factor 1×10^3. The convergence of the total pressure and total temperature for was manually observed for each of the optimized designs.

3.3 Optimization

The designs are developed using a single-objective, multivariate Bayesian optimization framework based on the `BO_GP` code[11]. The optimization loop consists of six steps:

1. Calculate geometry inputs using the Bayesian optimization model based on the existing data
2. Generate the duct geometry from the geometry inputs
3. Create a computational mesh
4. Solve for the flow field
5. Post-process the results to extract the target quantity
6. Add the target quantity to the database

The loop is then repeated until the optimization is considered sufficiently converged.

The optimization is used to sweep the area ratio of the heat exchanger for a constant duct length, and the duct length for a constant area ratio. The swept points are shown in Table 3.3.

Table 3.3: Swept area ratio (AR) and corresponding normalized duct length changes ($\Delta R/L$) used in the optimization process.

	Conventional Design					Aggressive Design		
AR	2.5	3	3.5	4	4	4	4	4
$\Delta R/L$	0.3	0.3	0.3	0.3	0.2	0.4	0.5	0.6

3.3.1 Optimization parameters

In each optimization case the area ratio and length of the duct was fixed. This left the position of the heat exchanger, the inclination of the heat exchanger and the eight Bezier control points be optimized. The optimization parameters and their allowed ranges are shown in Table 3.4. Increased values for λ_1 and λ_2 were used to allow for a more expressive diffusing duct.

Table 3.4: Ranges of the optimization variables used in the study.

Variable	**Range**
x_{mid}	[0.275, 0.725]
r_{mid}	[0.3, 0.8]
κ, deg	[10, 60]
λ_1 - λ_2	[0.05, 0.75]
λ_3 - λ_8	[0.05, 0.5]

3.3.2 Target function

The goal of the optimization is to minimize the total pressure drop over the duct while maintaining a set temperature drop. Given the inlet temperature of 13 °C and the water temperature of 5 °C a target temperature drop of $\Delta T_{\text{target}} = 10\,°\text{C}$ was

chosen. This is expected to return a heat-exchanger design that will result in a total pressure drop of roughly 1 %, which ensures that the experimental facility can drive the flow at the simulated mass flow.

The objective function $r(\mathbf{q})$ is defined as the total pressure drop between the inlet and the outlet:

$$r(\mathbf{q}) = \frac{p_{0,inlet} - p_{0,outlet}}{p_{0,inlet}} \tag{3.7}$$

where $p_{0,inlet}$ and $p_{0,outlet}$ is the mass averaged total pressure at the inlet and outlet of the air domain respectively. The stopping criterion for the optimization was 500 iterations.

3.4 Validation cases

The CFD model was simulated against two different diffuser geometries. Brief descriptions of the diffuser geometries and boundary conditions are provided in the two subsections below. The metric used to validate both ducts was the pressure recovery coefficient, C_{pr}, was used to compare the data between the CFD and the experimental results. It is a measure of how much dynamic pressure is converted into static pressure and is defined as

$$C_{pr} = \frac{p_e - p_t}{p_{0,t} - p_t} \tag{3.8}$$

where the subindex e corresponds to the diffuser exit and subindex t corresponds to the throat just ahead of the diffuser. These static pressures were calculated through area averaging while the total pressure was calculated through mass flow averaging.

3.4.1 Conical diffuser

Experimental data for conical diffusers with an inlet Mach number of 0.4 and a Reynolds number of 227,000 was obtained from [12]. The diffusers were parametrized by the ratio between the length of the duct and the throat diameter L/D_t, the area ratio AR, and the blockage ratio B_T. The numerical setup and mesh settings is identical to that described for the air side of the diffuser, Section 3.2.1.

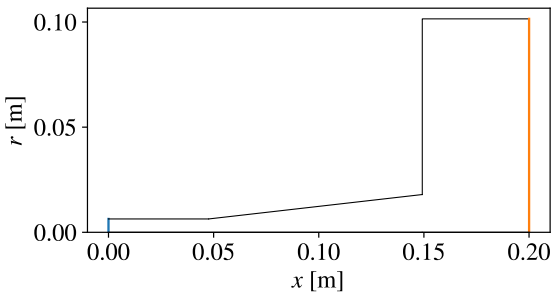

Figure 3.6: Meridional view of a conical diffuser with $AR = 8$, $L/D = 8$ and an inlet length that gives $B_T = 3\%$.

The geometry consists of an inlet tube which is used to build up a boundary layer to obtain the wanted blockage ratio, followed by the diffuser duct and a discharge plenum. The values used match the experimental setup, with the throat diameter being equal to $D_t = 1.27\,\text{cm}$ and the plenum diameter being equal to $20.3\,\text{cm}$.

The studied set of ducts consisted of two blockage ratios, 3% and 12%, two area ratios, 4 and 8, and lengths spanning from $L/D = 4$ to $L/D = 24$. An example geometry for $B_T = 3\%$, $L/D = 8$ and $AR = 8$ is shown in Figure 3.6.

3.4.2 Annular diffuser

Experimental data for annular diffusers with an inlet Mach number of 0.2 and a Reynolds number of 600,000 was obtained from [13]. The diffusers consisted of two parallel slanted walls which due to the axisymmetry diffuses the flow when increasing the mean radius.

The geometry used was parametrized through the ratio between the average wall length and the inlet hydraulic diameter $\bar{L}/D_h$, the blockage ratio B_T and the slope of the parallel walls ϕ. The investigated ducts had a blockage ratio of 2%, a slope of 15° and lengths spanning $\bar{L}/D_h = 2.28$ to $\bar{L}/D_h = 13.1$. An example duct with $\bar{L}/D_h = 5.66$ is shown in Figure 3.7.

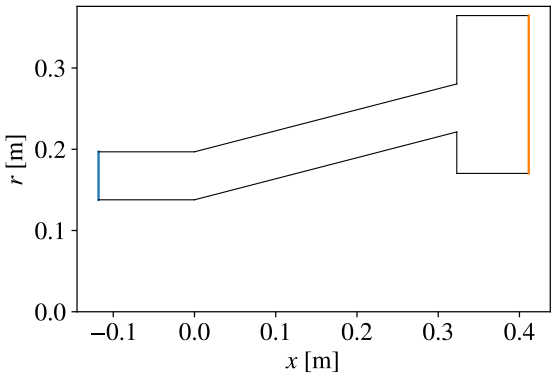

Figure 3.7: An annular diffuser used for validation with $\bar{L}/D_h = 5.66$. The inlet is shown in orange, and the outlet in black.

4
Results and discussion

This chapter will present and discuss the results from the validation case, the mesh convergence study, the optimization campaign and the non-isotropic heat exchanger case study.

4.1 Validation cases

The two sections below present the results from the validation study, as described in Section 3.4.

4.1.1 Conical Duct

Figures 4.1 present the pressure recovery coefficient C_{pr} as a function of the ratio between duct length and inlet diameter for conical diffusers with area ratios of 4 and 8, respectively. The solid lines represent CFD predictions, while the dashed lines correspond to experimental data from [12].

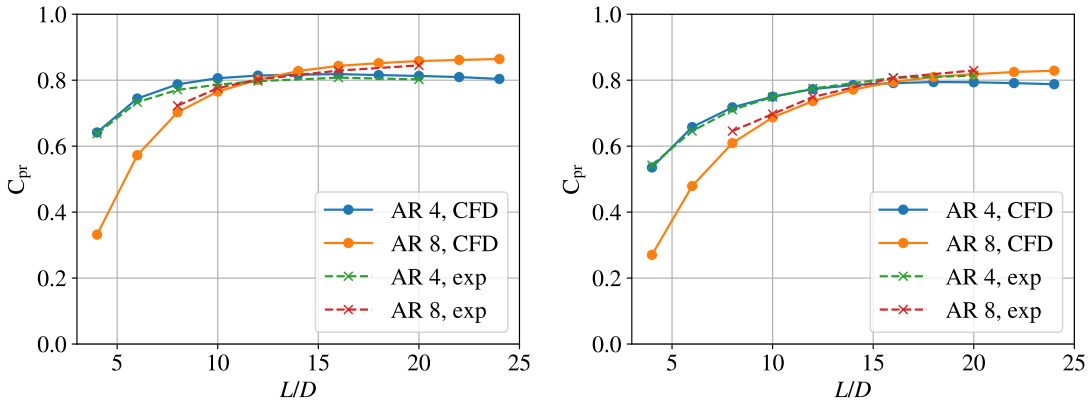

(a) $B_T = 3\%$. **(b)** $B_T = 12\%$.

Figure 4.1: Pressure recovery coefficient against the ratio between duct length and inlet diameter. (a): 3% inlet blockage ratio, (b): 12% inlet blockage ratio.

The results demonstrate that the CFD model accurately captures the diffusive behavior of short conical ducts. Notably, the simulations also reproduce the reduction in pressure recovery associated with higher blockage ratios. This increases the trustworthiness of the results of the optimization campaign as the inlet boundary

conditions used produced velocity profiles at the inlet with a blockage ratio of about 24 %.

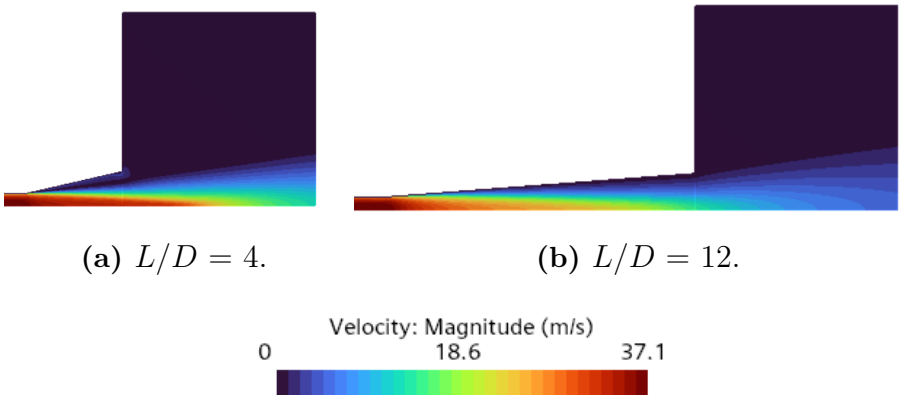

(a) $L/D = 4$. **(b)** $L/D = 12$.

Figure 4.2: Pressure recovery coefficient against the ratio between duct length and inlet diameter for two ducts with $AR = 8$ and $B_T = 12\%$.

The velocity fields for geometries with $B_T = 12\%$, AR = 4 and $L/D = 4$ or $L/D = 12$ are shown in Figure 4.2. The short duct shows significant separation, however as the Figure 4.1 showed the diffusive effects of the ducts are still matching well between the experimental and numerical datasets.

4.1.2 Annular duct

Figures 4.3 present the pressure recovery coefficient C_{pr} as a function of the ratio between duct length and inlet diameter for the annular diffuser. The solid line is the CFD results while the dashed line is experimental data from [13]. The figures shows an over prediction in the diffusive capacity of the duct.

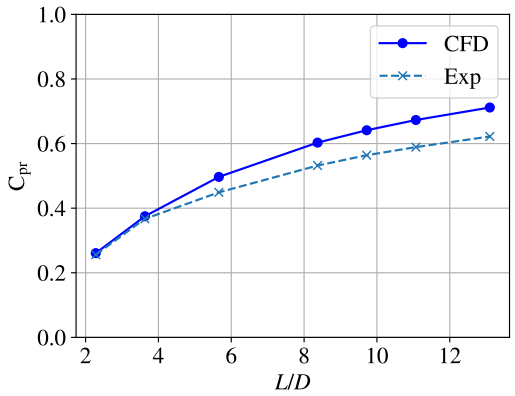

Figure 4.3: Pressure recovery coefficient against the ratio between duct length and inlet diameter for the annular duct.

The annular case was run without an exit plenum, and the outlet was instead placed at the diffuser exit. This was due to unsteady flow behavior in the annular

plenum which was not observed in the conical case, due to the stabilizing effect of the axis boundary condition. This could be an explanation for why the performance is overestimated, which points to the need of transient methods being needed to accurately estimate the diffusive properties in unsteady flows.

4.2 Convergence

This section presents the mesh convergence study as well as the solution convergence of the CFD simulations.

4.2.1 Mesh convergence

A mesh convergence study was performed using a representative duct geometry, illustrated in Figure 4.4, to evaluate the sensitivity of the simulation results to mesh resolution. The mesh size varied from 30,000 to 240,000 cells, and the total pressure drop between the inlet and outlet—normalized by the value obtained using the finest mesh—was used as the convergence metric. The results are presented in Figure 4.5. Based on the observed trend, the third finest mesh was selected for all subsequent simulations, as it provided an acceptable level of accuracy while substantially reducing computational cost, which was required by the optimization.

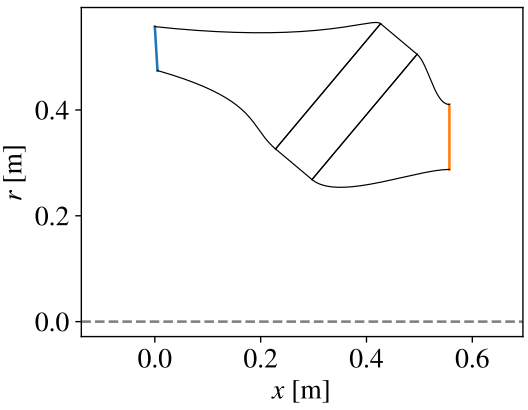

Figure 4.4: The geometry used in the mesh convergence study.

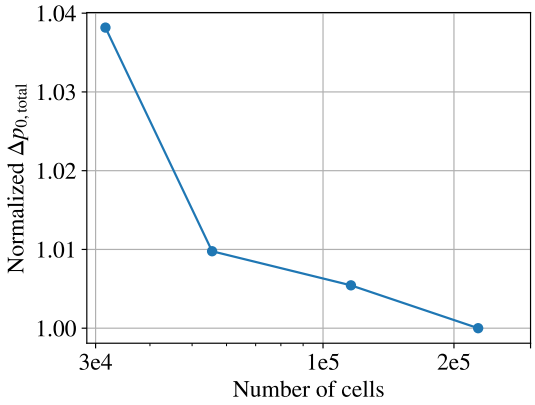

Figure 4.5: Normalized total pressure drop vs. number of cells in the mesh.

4.2.2 Solution convergence

The convergence of the total pressure drop, here normalized by inlet total pressure, as well as the temperature drop for the $AR = 4$, $\Delta R/L = 0.6$ duct are shown in Figures 4.6. The sharp increases located at iteration 400 corresponds to when the updating of χ is turned on. The convergence histories for all of the optimized designs followed the same trend: a sharp spike at 400 iterations followed by a smooth convergence to a final value with no oscillations observed. The convergence histories from other cases are omitted for brevity due to this similarity.

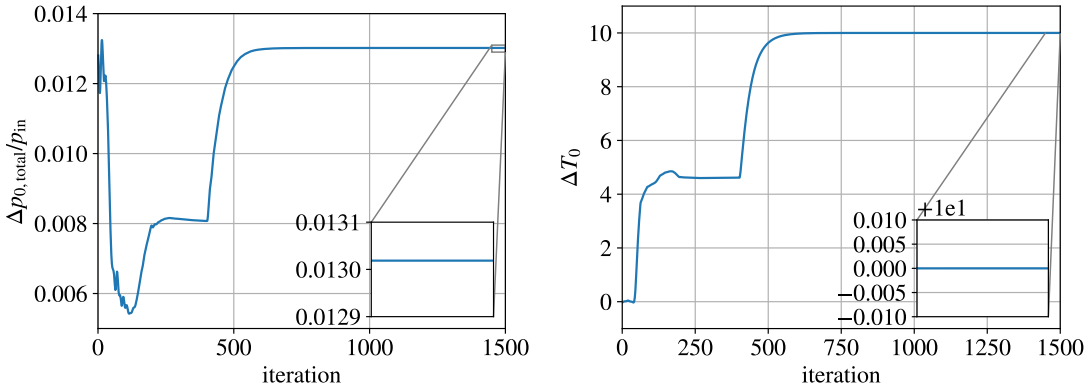

(a) Total pressure **(b)** Total temperature

Figure 4.6: Figures showing the convergence history for the total pressure and temperature drops.

4.3 Optimization results

This section presents the results from the optimization study. The results are split up into two parts, a sweep of AR for a constant duct length (Section 4.3.1) and a sweep of duct length for a constant AR (Section 4.3.2).

4.3.1 Effects of area ratio on performance

The effects of area ratio on performance were investigated by fixing $\Delta R/L = 0.3$ and optimizing the duct to minimize the duct inlet to outlet total pressure drop for different area ratios. This was done for fixed values of area ratios between 2.5 and 4.

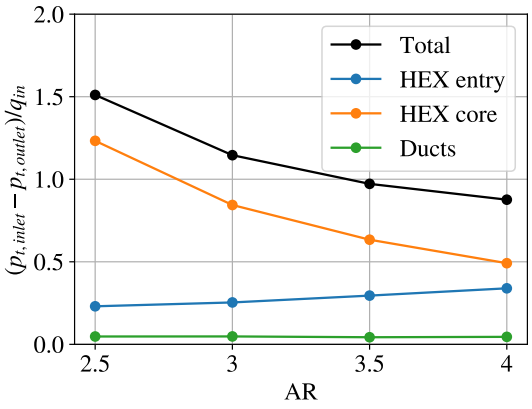

Figure 4.7: Total, HEX entry, HEX core and duct losses against area ratio for the optimal designs.

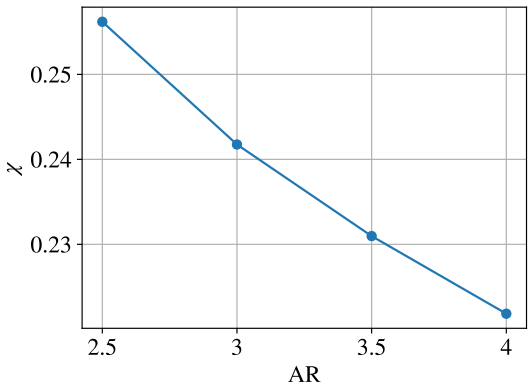

Figure 4.8: The value of χ, which correlates with fin density, against area ratio for the optimal designs.

Figure 4.7 shows that a larger area ratio gives lower overall losses. As the area ratio increases the HEX core losses decrease while the HEX entry losses increase.

The duct losses are largely negligible in all configurations.

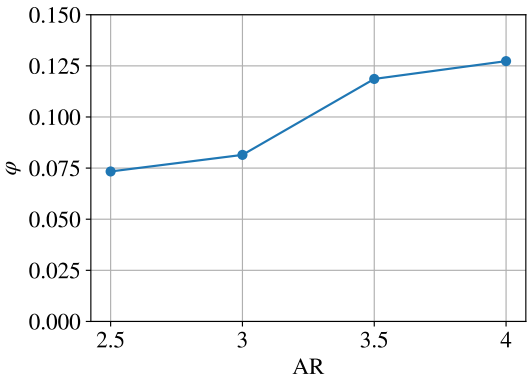

Figure 4.9: Velocity magnitude non-uniformity at the heat exchanger inlet.

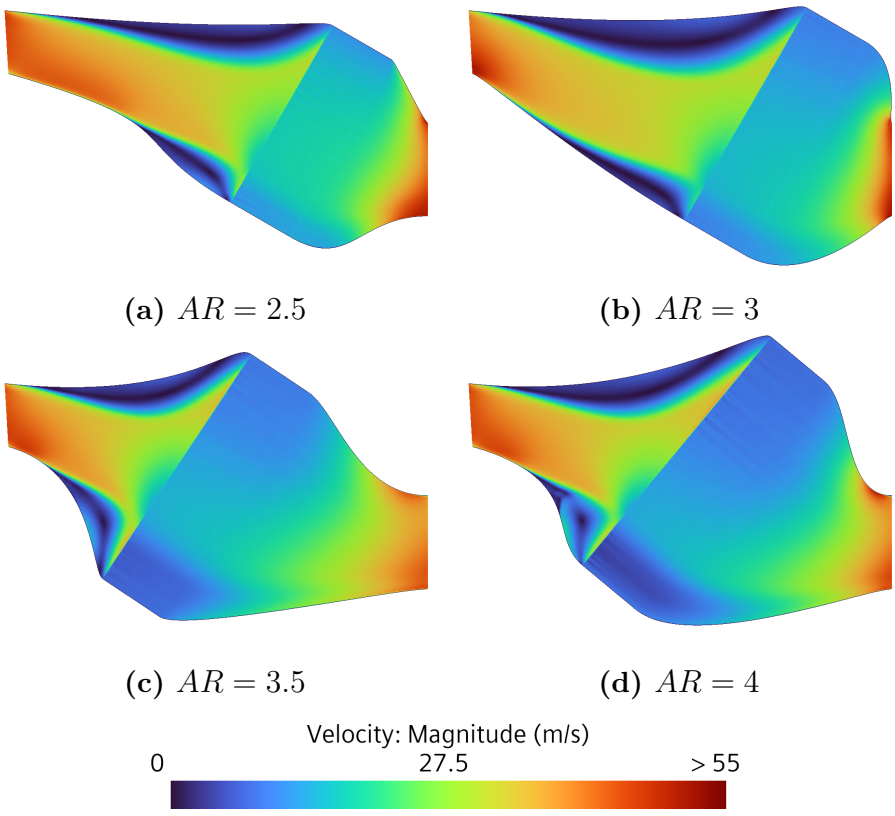

(a) $AR = 2.5$ **(b)** $AR = 3$

(c) $AR = 3.5$ **(d)** $AR = 4$

Figure 4.10: Velocity fields for the four optimized ducts in the area ratio sweep.

The reduction in losses over the HEX core is driven by the reduction of losses in the heat exchanger itself. This reduction is due to lower velocities through the heat exchanger, seen in Figure 4.10, as well as a lower fin density as shown in Figure 4.8. Lower velocities reduce the losses through the core as pressure losses scale with the velocity square while heat transfer is closer to linear in velocity (as seen in Equations 2.17 and 2.9 respectively).

The losses over the HEX entry are largely due to the finned structures effectively removing the velocity in the x'-direction due to the large pressure sink term in that direction. As the area ratio increases these losses also increase as the duct is unable to diffuse and turn the flow as much, which is also seen in an increase in the non-uniformity, Figure 4.9.

Observing the velocity fields, Figure 4.10, shows a clear trend: the optimal design always favors a jet of fluid which impacts the heat exchanger inlet. The jet spreads out across the entire interface which showcases the diffusive capacity of the heat exchanger itself. This is a core finding as previous work expected optimal designs to increase the diffusion by tilting the heat exchanger more relative to the inlet which reduces the effective area of the inlet duct which increases entry losses but also increases velocity magnitude non-uniformity [4].

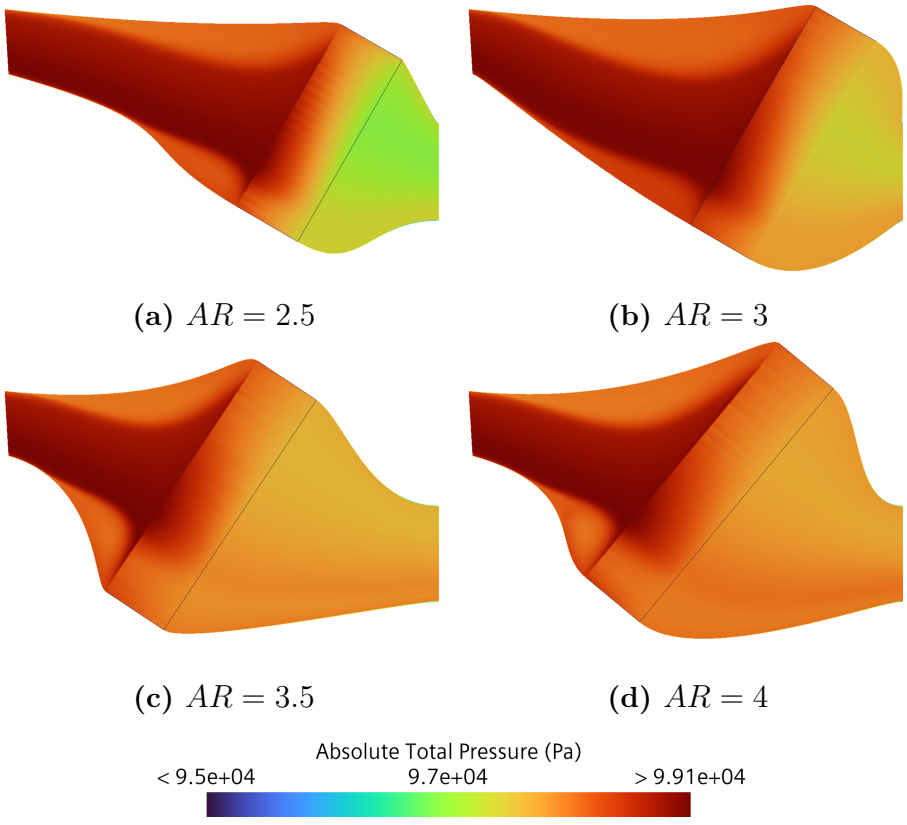

(a) $AR = 2.5$ **(b)** $AR = 3$

(c) $AR = 3.5$ **(d)** $AR = 4$

Figure 4.11: Total pressure fields for the four optimized ducts in the area ratio sweep.

The total pressure distributions presented in Figure 4.11 clearly demonstrate increased pressure losses in ducts with lower area ratios. These results also highlight distinct discontinuities in total pressure across the heat exchanger, particularly in regions adjacent to the walls. At the center of the heat exchanger, the flow remains predominantly aligned with the y'-direction, thereby minimizing the influence of the source term in the x'-momentum equation. As a result, total pressure is more uniformly preserved at the heat exchanger entry, yielding a relatively smooth pressure field. In contrast, near the duct walls, the flow exhibits a substantial velocity compo-

nent in the x'-direction. Consequently, the associated dynamic pressure is dissipated more significantly, leading to the discontinuities observed in the total pressure field.

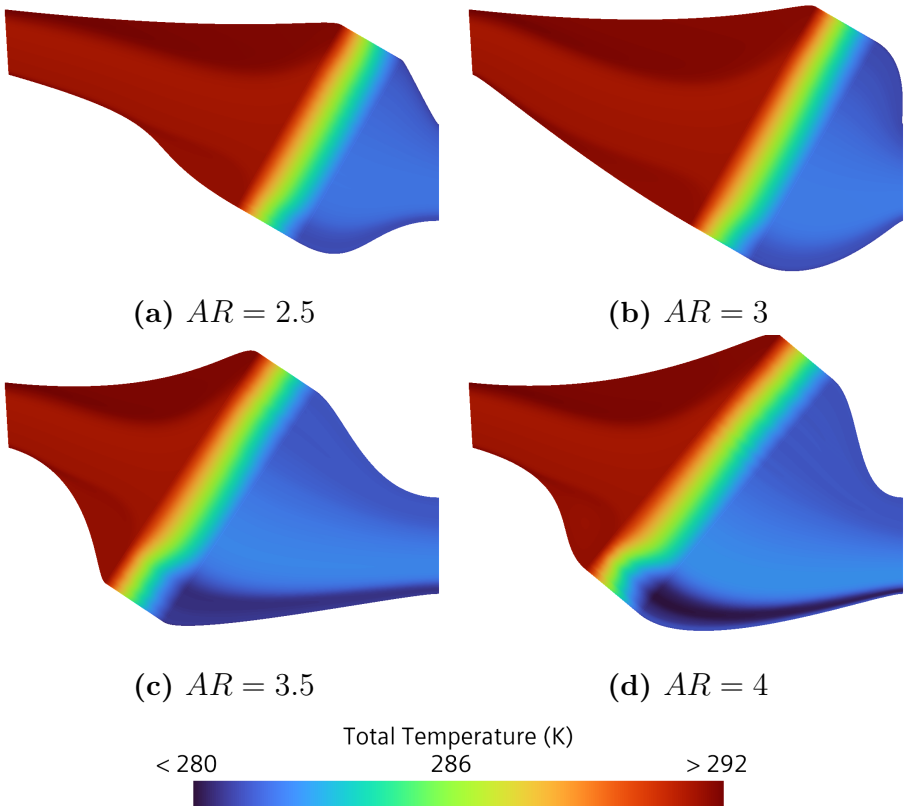

(a) $AR = 2.5$ **(b)** $AR = 3$

(c) $AR = 3.5$ **(d)** $AR = 4$

Figure 4.12: Temperature fields for the four optimized ducts in the area ratio sweep.

The total temperature fields, Figure 4.12, shows a uniform temperature decrease in the $AR = 2.5$ and $AR = 3$ case, while the larger area ratios show cold spots. These cold spots are due to flow stagnation in the heat exchanger which allows the flow to reach the temperature of the cold side. This behavior indicates that the heat exchanger model is functioning as intended, since a simpler model employing a constant volumetric heat sink would produce unrealistically low temperatures.

4.3.2 Effects of duct length on performance

The effects of area ratio on performance were investigated by fixing $AR = 4.0$ and optimizing the duct to minimize the duct inlet to outlet total pressure drop for different area ratios. This was done for fixed values of $\Delta R/L$ between 0.2 and 0.6.

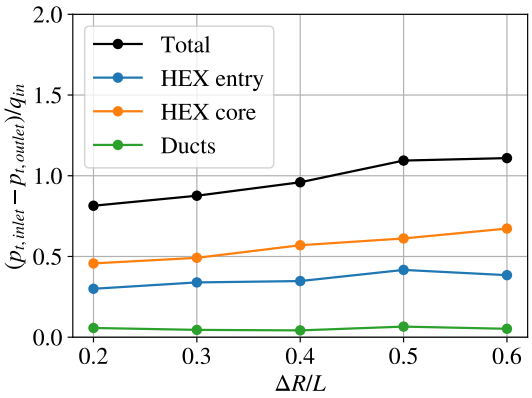

Figure 4.13: Total, HEX entry, HEX core and duct losses against area ratio for the optimal designs.

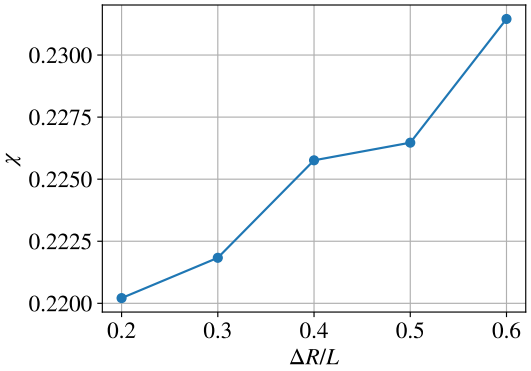

Figure 4.14: The value of χ, which correlates with fin density, against area ratio for the optimal designs.

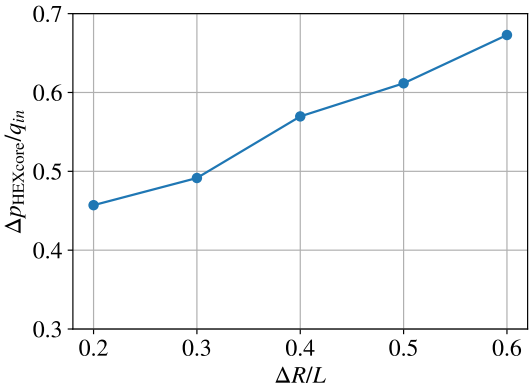

Figure 4.15: Heat exchanger core pressure losses against $\Delta R/L$ for the optimal designs.

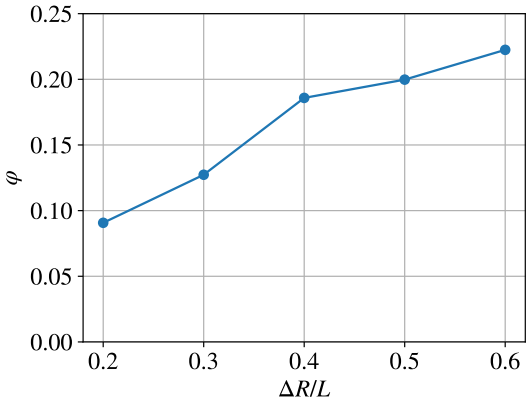

Figure 4.16: The value HEX inlet-normal velocity uniformity $\Delta R/L$ for the optimal designs.

Figure 4.13 show the distribution of losses as the length of the duct decreases. A shorter duct results in increased HEX core losses, as well as increased entry losses for all duct lengths except the shortest configuration. One explanation for this change in loss distribution is that there are different types of configurations with similar performance, making it difficult for a clear trend to emerge as the search space for the optimizer becomes flat. Another explanation for this change in behavior could that the optimization is not fully converged for all the designs.

Looking at the isolated HEX core losses, Figure 4.15, and the velocity uniformity, Figure 4.16, there is a clear correlation. As the non-uniformity increases the losses

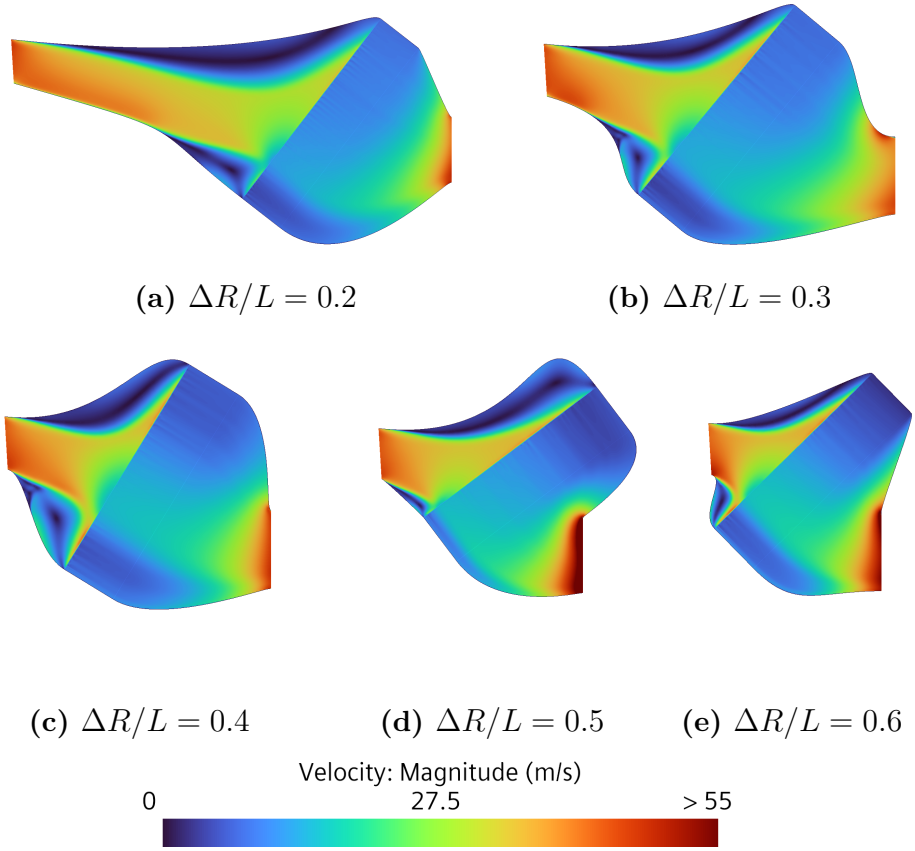

(a) $\Delta R/L = 0.2$ **(b)** $\Delta R/L = 0.3$

(c) $\Delta R/L = 0.4$ **(d)** $\Delta R/L = 0.5$ **(e)** $\Delta R/L = 0.6$

Figure 4.17: Velocity magnitude fields for the five optimized ducts in the $\Delta R/L$ sweep.

increase. This is due to the pressure drop scaling with the square of the velocity, as discussed in the section above, which causes a less uniform flow through the heat exchanger core to give rise to increased losses.

The velocity fields in figure 4.17 share similarities to the ducts in the AR-sweep. All designs feature separation regions to some degree. The least aggressive design, $\Delta R/L = 0.2$, features a partially-attached flow on the hub diffuser wall, similarly to the least aggressive design in the area ratio sweep.

As the ducts become very short the separation regions start to diminish as there's simply no space for them. While the shorter ducts do struggle with diffusion, seen through increased non-uniformity, they also struggle to turn the flow which is seen through the increased HEX entry losses. Future studies could look to try and use the heat exchanger surfaces themselves as a means to diffuse and turn the flow inside the duct.

The total temperature fields also illustrate how diffusive capacity of the designs decreases as the ducts become shorter. This is seen through the increase of cold spots throughout the heat exchanger.

The $\Delta R/L = 0.5$ duct shows a large bulge on the shroud side of the heat exchanger, which gives rise to a large cold spot. The shorter $\Delta R/L = 0.6$ duct is instead moved such that the heat exchanger is more centered relative to the incom-

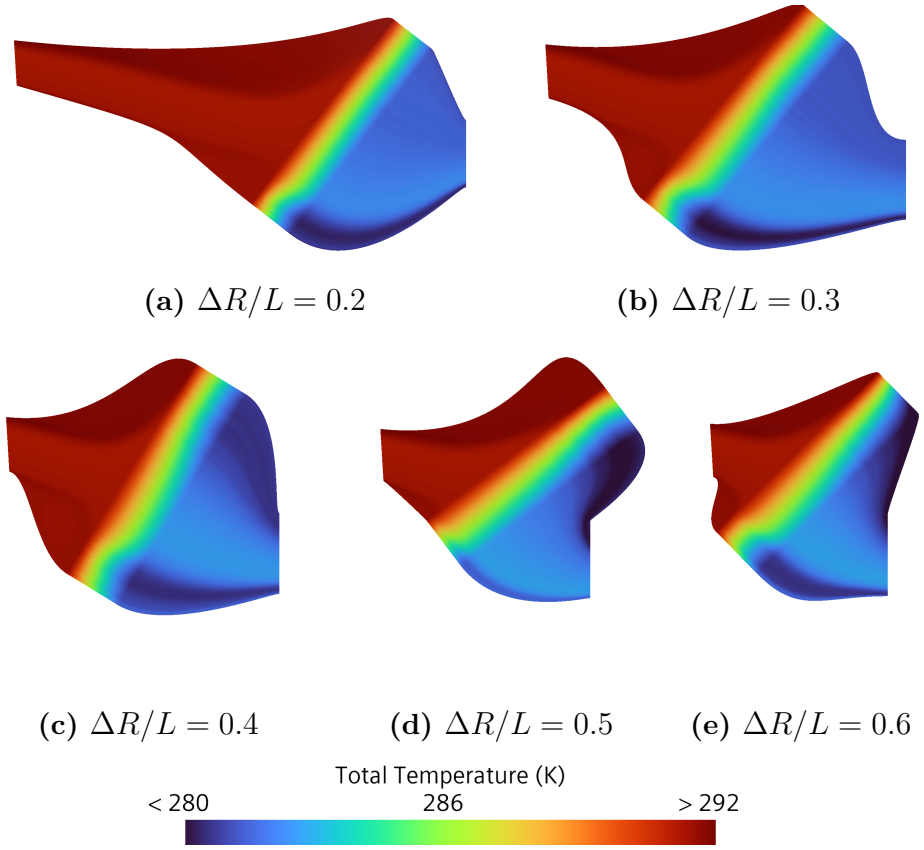

(a) $\Delta R/L = 0.2$ **(b)** $\Delta R/L = 0.3$

(c) $\Delta R/L = 0.4$ **(d)** $\Delta R/L = 0.5$ **(e)** $\Delta R/L = 0.6$

Figure 4.18: Total temperature fields for the five optimized ducts in the $\Delta R/L$ sweep.

ing fluid jet which instead gives rise to two smaller cold spots, one at the hub and one at the shroud. This could be an indicator that the optimization is not fully converged, but it could also be an indicator that different loss distributions can both be close to optimal when minimizing the total losses.

4.4 Isotropic heat exchanger

To assess the effect of heat exchanger anisotropy, simulations were performed using the previously optimized geometry for the case with $\Delta R/L = 0.3$ and $AR = 3$. Three configurations were compared:

1. A finned heat exchanger, with fin normals aligned along the x'-direction.
2. An isotropic heat exchanger, where the fins are arranged tangentially to the plane and pressure losses are applied isotropically in the $x - r$ plane.
3. A baseline case with no heat exchanger.

All configurations used the same geometry to isolate the effects of the heat exchanger characteristics.

Table 4.1 presents the resulting losses, flow non-uniformity, and the effectiveness parameter χ. The velocity fields for the three cases are shown in Figure 4.19, highlighting the differences in flow behavior.

Table 4.1: Aerothermal performance for different heat exchanger types.

Heat exchanger type	**Finned**	**Isotropic**	**No HEX**
ΔT	10 K	10 K	0 K
$\Delta p_0/q_{\text{in}}$	1.146	1.159	0.037
$\Delta p_{0,\text{HEX entry}}/q_{\text{in}}$	0.254	0.143	N/A
$\Delta p_{0,\text{HEX core}}/q_{\text{in}}$	0.844	0.97	N/A
$\Delta p_{0,\text{ducts}}/q_{\text{in}}$	0.048	0.046	N/A
Non-uniformity	0.081	0.226	0.565
χ	0.242	0.234	N/A

The analysis of aerothermal performance presented in Table 4.1 reveals several notable insights. The pressure losses for the finned and isotropic heat exchanger configurations are nearly identical, differing by about 1 %. In the isotropic case, the reduction in entry losses is traded for higher core losses, for a low net change in performance. This reduction in entry losses arises from the absence of fins, which in the finned configuration removes a large amount of dynamic pressure.

However, the lack of fins also removes the constraint that forces the fluid to follow the shortest possible path through the heat exchanger, along the y'-axis. Consequently, while entrance losses are reduced in the isotropic configuration, they are not entirely eliminated. This is primarily due to the increased freedom of the fluid to traverse significant distances in the x'-direction within the entry region. Furthermore, the fluid tends to follow a longer trajectory through the core of the heat exchanger, which contributes to higher core losses. This occurs despite the reduction in pressure drop that results from a lower value of χ.

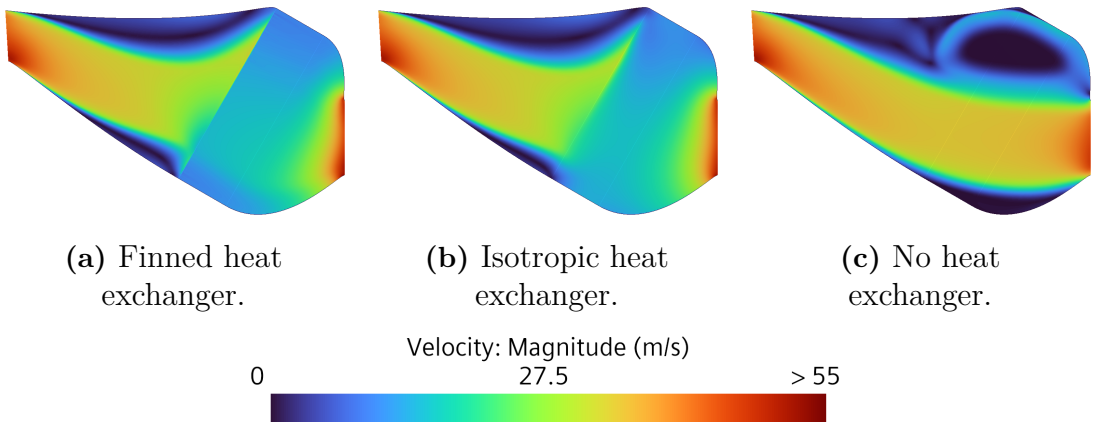

(a) Finned heat exchanger.

(b) Isotropic heat exchanger.

(c) No heat exchanger.

Figure 4.19: Velocity fields for the optimized $\Delta R/L = 0.3$, $AR = 3$ duct for different styles of heat exchangers.

This difference in flow behavior is further illustrated by the flow field visualizations of the two configurations in Figure 4.19a and 4.19b. In the finned heat

exchanger, the flow remains aligned with the y'-axis, as the fins restrict lateral diffusion and inhibit mixing. In contrast, the isotropic configuration shows significant mixing inside the heat exchanger which results in a smoother velocity field.

The velocity field for the case without a heat exchanger, Figure 4.19c, clearly illustrate the diffusive influence of the heat exchangers on the flow behavior. In the absence of a heat exchanger, the flow exhibits the characteristics of a pure jet, with minimal diffusion and a narrow velocity profile confined to the central region of the duct. In contrast, the presence of heat exchangers, both finned and isotropic, promotes greater diffusion, resulting in a broader distribution of the flow across the duct.

5
Conclusion

This thesis has demonstrated the effectiveness of using coupled models with optimization techniques to conduct rapid design studies. By constraining the designs to achieve the same thermal load the performance comparisons can be simplified and consistency can be ensured across design iterations. This allows for rapid design evaluations and is made possible by the embedding of aerothermal performance calculations of heat exchangers directly within the CFD solver.

The main conclusion from the parameter sweeps is that higher area ratios and longer ducts reduce aerodynamic losses. Across all configurations, highly separated flow regions were observed, yet the overall level of diffusion remained high. This indicates that the dominant source of diffusion is the heat exchanger itself, rather than the surrounding duct.

Additionally, the study found that finned and isotropic heat exchangers yielded similar performance when placed in the same duct geometry. This suggests that the fins are not the primary driver of diffusion. Instead, the dominant mechanism appears to be the velocity-dependent pressure drop induced by the heat exchanger matrix.

Future work could leverage the computational tool developed in this thesis to enable new strategies for duct and heat exchanger design. Operating within a continuum framework, the tool supports the evaluation of complex heat exchanger geometries that go beyond simple shapes such as the square diffuser in this work. This flexibility opens up opportunities to explore integrated configurations in which the heat exchanger extends into the duct's diffusing section, varying fin angles throughout the geometry and non-uniform heat exchanger geometries. Such designs have the potential to redistribute aerodynamic diffusion more effectively between the duct and heat exchanger, potentially yielding beneficial synergies through reduced flow separation and improved flow control.

Bibliography

[1] European Commission. *The European Green Deal*. COM(2019) 640 final. Brussels: European Commission, Dec. 2019. URL: https://eur-lex.europa.eu/legal-content/EN/TXT/?uri=CELEX%3A52019DC0640.

[2] European Commission. *Reducing emissions from aviation*. Accessed: 2025-06-03. 2025. URL: https://climate.ec.europa.eu/eu-action/transport-decarbonisation/reducing-emissions-aviation_en.

[3] Alexandre Capitao Patrao et al. "The heat transfer potential of compressor vanes on a hydrogen fueled turbofan engine". In: *Applied Thermal Engineering* 236 (Jan. 2024), p. 121722. ISSN: 1359-4311. DOI: 10.1016/j.applthermaleng.2023.121722. URL: http://dx.doi.org/10.1016/j.applthermaleng.2023.121722.

[4] Alexandre Capitao Patrao et al. "Compact heat exchangers for hydrogen-fueled aero engine intercooling and recuperation". In: *Applied Thermal Engineering* 243 (Apr. 2024), p. 122538. ISSN: 1359-4311. DOI: 10.1016/j.applthermaleng.2024.122538. URL: http://dx.doi.org/10.1016/j.applthermaleng.2024.122538.

[5] Alexandre Capitao Patrao, Isak Jonsson, and Carlos Xisto. "Compact Heat Exchangers With Curved Fins for Hydrogen Turbofan Intercooling". In: *Journal of Engineering for Gas Turbines and Power* 146.11 (July 2024). ISSN: 1528-8919. DOI: 10.1115/1.4065887. URL: http://dx.doi.org/10.1115/1.4065887.

[6] Petter Miltén et al. "Generalized Method for the Conceptual Design of Compact Heat Exchangers". In: *Journal of Engineering for Gas Turbines and Power* 146.11 (Aug. 2024). ISSN: 1528-8919. DOI: 10.1115/1.4065922. URL: http://dx.doi.org/10.1115/1.4065922.

[7] William M Kays and A L London. *Compact Heat Exchangers*. 2nd ed. McGraw-Hill Companies, Oct. 1964.

[8] Frank P Incropera et al. *Fundamentals of heat and mass transfer*. en. 6th ed. Nashville, TN: John Wiley & Sons, Sept. 2006.

[9] Y. Morita et al. "Applying Bayesian optimization with Gaussian process regression to computational fluid dynamics problems". In: *Journal of Computational Physics* 449 (Jan. 2022), p. 110788. ISSN: 0021-9991. DOI: 10.1016/j.jcp.2021.110788. URL: http://dx.doi.org/10.1016/j.jcp.2021.110788.

[10] Isak Jonsson et al. “Design and Pre-Test Evaluation of a Low-Pressure Compressor Test Facility for Cryogenic Hydrogen Fuel Integration”. In: *Volume 2A: Turbomachinery — Axial Flow Fan and Compressor Aerodynamics*. GT2021. American Society of Mechanical Engineers, June 2021. DOI: 10.1115/gt2021-58946. URL: http://dx.doi.org/10.1115/GT2021-58946.

[11] Saleh Rezaeiravesh. *BO-GP*. Accessed 2025-05-06. Dec. 2, 2022. URL: https://github.com/KTH-Nek5000/BO_GP.

[12] F. X. Dolan and Jr. Runstadler P. W. *Pressure Recovery Performance of Conical Diffusers at High Subsonic Mach Numbers*. Contractor Report NASA-CR-2299. TN-165. Washington, D.C.: NASA, July 1973. URL: https://ntrs.nasa.gov/citations/19730022195.

[13] G. Sovran and E. D. Klomp. “Experimentally Determined Optimum Geometries for Rectilinear Diffusers with Rectangular, Conical or Annular Cross-Section”. In: *Fluid Mechanics of Internal Flow*. Ed. by G. Sovran. Amsterdam: Elsevier Publishing Co., 1967, pp. 270–319.

DEPARTMENT OF MECHANICS AND MARITIME SCIENCES
CHALMERS UNIVERSITY OF TECHNOLOGY
Gothenburg, Sweden
www.chalmers.se

CHALMERS
UNIVERSITY OF TECHNOLOGY